1 **Structure, activity and inhibition of human TMPRSS2, a protease implicated in SARS-**
2 **CoV-2 activation**

3 Bryan J. Fraser#, Serap Beldar#, Almagul Seitova, Ashley Hutchinson, Dhiraj Mannar, Yanjun
4 Li, Daniel Kwon, Ruiyan Tan, Ryan P. Wilson, Karoline Leopold, Sriram Subramaniam, Levon
5 Halabelian*, Cheryl H. Arrowsmith*, François Bénard*
6 # equal contribution
7 *Corresponding

8

9 **ABSTRACT**

10 Transmembrane protease, serine 2 (TMPRSS2) has been identified as key host cell factor for
11 viral entry and pathogenesis of SARS-coronavirus-2 (SARS-CoV-2). Specifically, TMPRSS2
12 proteolytically processes the SARS-CoV-2 Spike (S) Protein, enabling virus-host membrane
13 fusion and infection of the lungs. We present here an efficient recombinant production strategy
14 for enzymatically active TMPRSS2 ectodomain enabling enzymatic characterization, and the
15 1.95 Å X-ray crystal structure. To stabilize the enzyme for co-crystallization, we pre-treated
16 TMPRSS2 with the synthetic protease inhibitor nafamosat to form a stable but slowly reversible
17 (15 hour half-life) phenylguanidino acyl-enzyme complex. Our study provides a structural basis
18 for the potent but non-specific inhibition by nafamostat and identifies distinguishing features of
19 the TMPRSS2 substrate binding pocket that will guide future generations of inhibitors to
20 improve selectivity. TMPRSS2 cleaved recombinant SARS-CoV-2 S protein ectodomain at the
21 canonical S1/S2 cleavage site and at least two additional minor sites previously uncharacterized.
22 We established enzymatic activity and inhibition assays that enabled ranking of clinical protease
23 inhibitors with half-maximal inhibitory concentrations ranging from 1.7 nM to 120 µM and
24 determination of inhibitor mechanisms of action. These results provide a body of data and
25 reagents to support future drug development efforts to selectively inhibit TMPRSS2 and other
26 type 2 transmembrane serine proteases involved in viral glycoprotein processing, in order to
27 combat current and future viral threats.

28

29 **SUMMARY PARAGRAPH**

30 Viruses hijack the biochemical activity of host proteins for viral invasion and replication.
31 Transmembrane protease, serine-2 (TMPRSS2) is a surface-expressed protease implicated in the
32 activation of influenza A, influenza B, and coronaviruses, including SARS-CoV-2, to drive
33 efficient infection of the lungs[1–5]. TMPRSS2 is an attractive target for antiviral therapies, as
34 inhibiting its proteolytic activity blocks efficient viral entry[5,6]. However, a structural and
35 biochemical understanding of the protease has remained elusive and no selective inhibitors are
36 available. We engineered on-demand activatable TMPRSS2 ectodomain and determined the 1.95
37 Å X-ray crystal structure of the stabilized acyl-enzyme after treatment with nafamostat, a protease
38 inhibitor under investigation as a COVID-19 therapeutic. The structure reveals unique features of
39 the TMPRSS2 substrate recognition pocket and domain architecture, and explains the potent, but
40 nonselective inhibition by nafamostat. TMPRSS2 efficiently cleaved the SARS-CoV-2 S protein
41 at the canonical S1/S2 site as well as two minor sites previously uncharacterized. We further
42 established a robust enzymatic assay system and characterized inhibition by two additional clinical
43 protease inhibitors under study for COVID-19, camostat and bromhexine. Our results provide a
44 body of data and reagents to enable ongoing drug development efforts to selectively inhibit
45 TMPRSS2 and other TTSPs involved in viral glycoprotein processing, in order to combat current
46 and future viral threats.

47 **MAIN**

48

49 **Production and structure of on-demand activatable TMPRSS2 ectodomain**

50 TMPRSS2 is a type 2 transmembrane serine protease (TTSP) comprised of an intracellular

51 domain, single-pass transmembrane domain, and a biologically active ectodomain with three

52 subdomains: a low density lipoprotein receptor type-A (LDLR-A) domain, a Class A Scavenger

53 Receptor Cysteine-Rich (SRCR) domain and a C-terminal trypsin-like serine peptidase (SP)

54 domain with a canonical Ser441-His296-Asp345 catalytic triad (Fig. 1a and e)[7,8]. As TMPRSS2 is

55 synthesized as a single-chain proenzyme, or zymogen, it requires cleavage at a conserved Arg255-

56 Ile256 peptide bond within its SRQSR255↓IVGGE activation motif (cleavage site denoted with

57 an arrow) to achieve full maturation of its enzymatic activity[8,9]. We achieved this in high yield by

58 replacing SRQSR255↓ with an enteropeptidase-cleavable DDDDK255↓ sequence to prohibit auto-

59 activation, allowing purification of a secreted form of the full TMPRSS2 ectodomain zymogen

60 from insect cells, analogous to a strategy used for the TTSP, matriptase (Methods)[10]. Subsequent

61 proteolytic activation with recombinant enteropeptidase afforded highly active, homogenous

62 TMPRSS2 to milligram yields and was accordingly named directed activation strategy TMPRSS2

63 (dasTMPRSS2; Fig. 1b; Extended Data Fig. 1). We determined the X-ray crystal structure of

64 dasTMPRSS2 refined to 1.95Å resolution after acylation of the catalytic Ser441 residue with

65 nafamostat, a broad-spectrum synthetic serine protease inhibitor[11]. We obtained clear electron

66 density for residues 149-491 spanning the SRCR and SP domains but not residues 109-148

67 containing the flexible LDLR-A domain responsible for linking the protease to the plasma

68 membrane (Fig. 1c). The engineered DDDDK255 activation motif was not resolved in the structure

69 but rather terminated in an unstructured loop, consistent with matured TMPRSS13 (6KD5) and

70 hepsin (1Z8G) structures containing their native activation motifs[12,13]. The newly exposed N-

71 terminal Ile256 of the SP domain formed a salt bridge with the side chain of Asp440, confirming

72 full maturation of the activation pocket, and taken together with the Cys244-Cys365 interdomain

73 disulfide, confirms that this structure represents the bioactive, stabilized form of the protease (Fig.
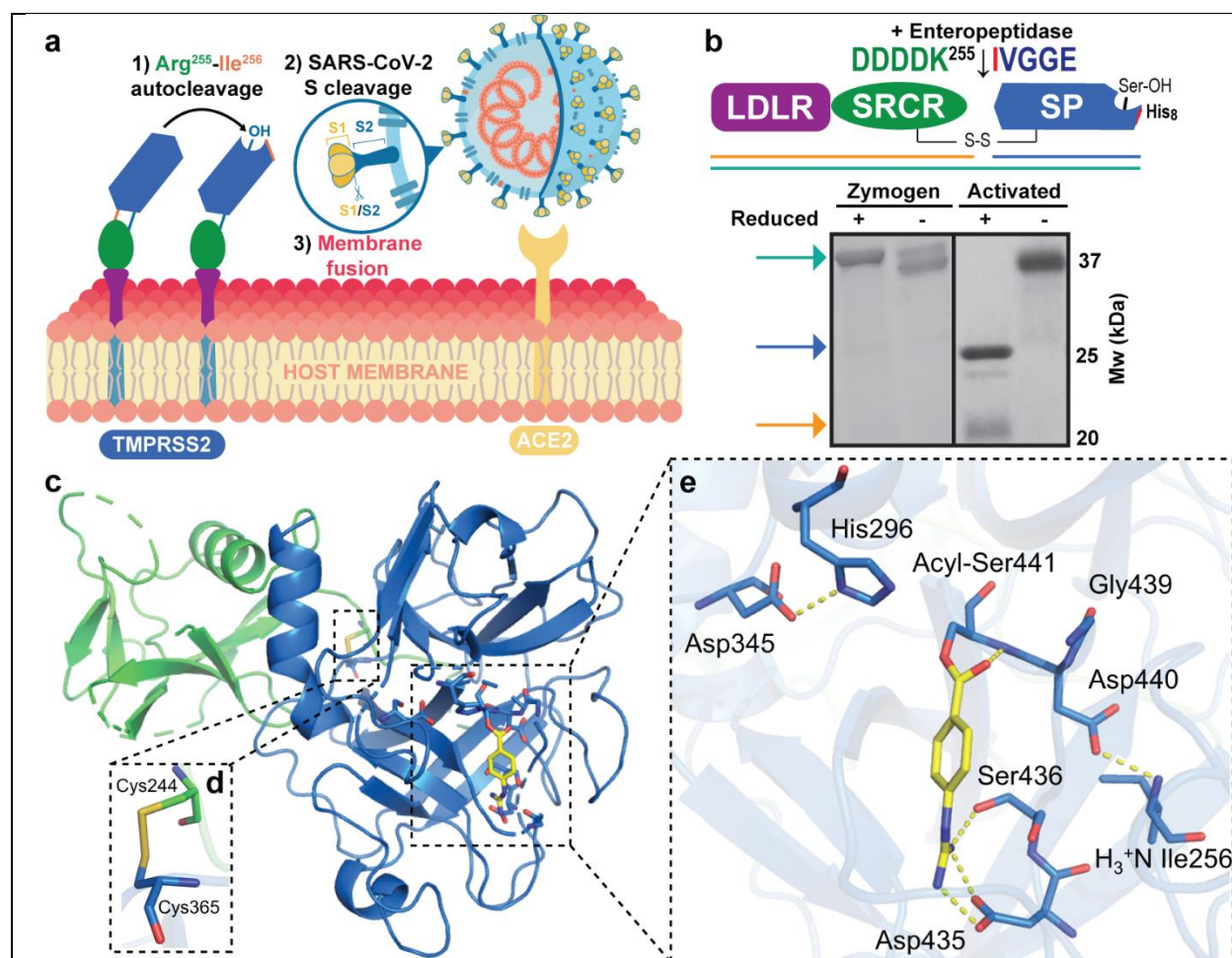
74 1d-e).

Figure 1. Engineered activation and structural characterization of stabilized TMPRSS2 ectodomain. a Full-length, membrane bound TMPRSS2 zymogen undergoes autocleavage activation at the Arg255-Ile256 peptide bond and the matured enzyme proteolytically processes SARS-CoV-2 Spike protein docked to the ACE2 receptor to drive viral membrane fusion. **b** Engineered recombinant TMPRSS2 ectodomain containing the low-density lipoprotein receptor type-A (LDLR) domain, a Class A Scavenger Receptor Cysteine-Rich (SRCR) domain and a C-terminal trypsin-like serine peptidase (SP) domain, features an enteropeptidase-cleavable DDDDK^{255} substitution to facilitate controlled zymogen activation. The non-catalytic (LDLR+SRCR) and catalytic (SP) chains are tethered by a disulfide bond and the activation status can be interrogated by SDS-PAGE under non-reducing and reducing (5% β-mercaptoethanol) conditions. **c** X-ray crystal structure of activated TMPRSS2 ectodomain pre-treated with nafamostat (yellow sticks). **d** The interdomain disulfide pair (Cys244-Cys365) maintains covalent attachment of the SRCR and SP domains. **e** Close-up view of the SP catalytic triad residues (His296, Asp345 and Ser441) and the post-activation Asp440:Ile256 salt bridge showing complete maturation of the protease. Nafamostat treatment results in phenylguanidino acylation of Ser441. Polar contacts are shown as yellow dashed lines.

75

76 **TMPRSS2 has a unique and accommodating substrate binding cleft**

77 The TMPRSS2 SP domain is highly conserved with all TTSPs and conforms to the canonical
78 chymotrypsin/trypsin fold with two six-stranded beta barrels converging to a central active site
79 cleft harboring the catalytic triad (Fig. 1c)[14]. Divergent protein substrate specificity of these closely
80 related proteases is conferred through highly variable, surface-exposed loops, denoted Loop A-E

81 and Loops 1-3 (Extended Data Fig. 2)[14]. Unique subsites formed on the face of the SP domain, S4-
82 S3-S2-S1-S1'-S2'-S3'-S4' recognize substrate P4-P3-P2-P1↓P1'-P2'-P3'-P4' amino acid
83 positions spanning the scissile bond (Fig 2a; Extended Data Fig 3a). To rationally assign these
84 subsites for TMPRSS2, we superposed the peptide-bound hepsin and TMPRSS13 SP domains
85 (40.1% and 41.4% sequence identity of their SP domains, respectively) belonging to the same
86 hepsin/TMPRSS subfamily as TMPRSS2. The S1 position of TMPRSS2 is occupied by the
87 phenylguanidino moiety of nafamostat, forming salt bridges with the highly conserved Asp435,
88 Ser436, and Gly464 residues in the same binding mode as the guanidino of P1 Arg residues
89 observed in hepsin and TMPRSS13 (Fig. 1e; Fig. 2a; Extended Data Fig. 3a). The TMPRSS2 S2
90 subsite has a distinguishing Lys342 residue that likely confers a preference for small and/or
91 electronegative P2 substrates, similar to the S2 Lys in enteropeptidase which prefers P2 Asp
92 residues[15]. The S3 and S4 subsites appear open to accommodate various P3 and P4 amino acids
93 and may make favorable receptor contacts with the respective Gln438 and Thr341 positions (Fig.
94 2a, Extended Data Fig. 3a). On the N-terminal side of the scissile bond, the buried S1' site appears
95 to accept small, hydrophobic P1' residues. Overall, the TMPRSS2 active site appears capable of
96 binding various substrate sequences with the strictest preference for the P1 and P2 positions.
97
98 Among TTSPs, the SP domain of TMPRSS2 uniquely possesses 3 disulfides and a single unpaired
99 cysteine residue, Cys379 (Extended Data Fig. 2b-d). In all other TTSPs this position forms a
100 disulfide bond with an additional Cys at the equivalent of Thr447, or both cysteines are absent.
101 This unpaired cysteine is conserved in feline, bovine, mouse, and rat TMPRSS2 orthologs
102 (Extended Data Fig. 2e). Furthermore, the unpaired Cys379 is bordered by an expansive 360 Å^2
103 patch of exposed hydrophobic surface area in our structure that may serve as an interaction hub
104 for TMPRSS2 binding partners (Extended Data Fig. 2b).
105
106 **The SRCR domain confers additional diversity for molecular recognition.**
107 The SRCR domain is found enriched in proteins expressed at the surface of immune cells as well
108 as in secreted proteins, and are thought to participate in protein-protein interactions and substrate
109 recognition[16]. The Class A SRCR domain of TMPRSS2 is located on the backside of the SP
110 domain away from the active site and is structurally similar to that of TMPRSS13 despite sharing
111 only 19% sequence identity (Fig. 2b). These two SRCR domains adopt a compact, globular fold
112 with similar orientations relative to their SP domains (Fig. 2b,c). The SRCR of hepsin (7.5%
113 sequence identity) diverges significantly from TMPRSS2/13 with three intra-domain disulfides
114 and a tighter SRCR:SP association dominated by complementary electrostatic patches and buried
115 surface area (Fig. 2c). These conformational differences may play a role in the orientation of the
116 SP domain relative to the plasma membrane as well as modulate activity through recognition or
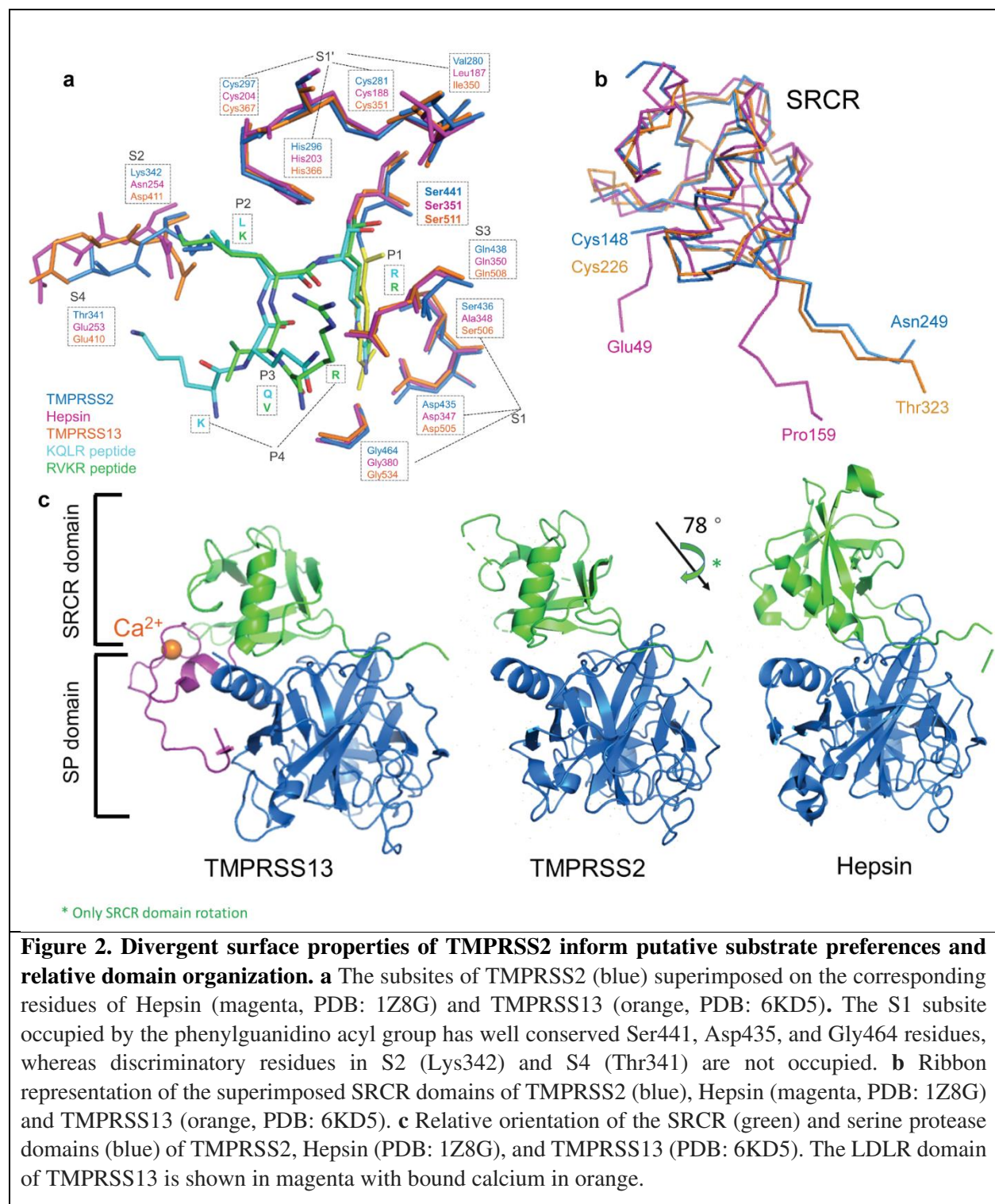117 recruitment of partner proteins.
118
119
120

121

Figure 2. Divergent surface properties of TMPRSS2 inform putative substrate preferences and relative domain organization. a The subsites of TMPRSS2 (blue) superimposed on the corresponding residues of Hepsin (magenta, PDB: 1Z8G) and TMPRSS13 (orange, PDB: 6KD5). The S1 subsite occupied by the phenylguanidino acyl group has well conserved Ser441, Asp435, and Gly464 residues, whereas discriminatory residues in S2 (Lys342) and S4 (Thr341) are not occupied. **b** Ribbon representation of the superimposed SRCR domains of TMPRSS2 (blue), Hepsin (magenta, PDB: 1Z8G) and TMPRSS13 (orange, PDB: 6KD5). **c** Relative orientation of the SRCR (green) and serine protease domains (blue) of TMPRSS2, Hepsin (PDB: 1Z8G), and TMPRSS13 (PDB: 6KD5). The LDLR domain of TMPRSS13 is shown in magenta with bound calcium in orange.

122

TMPRSS2 displays robust in vitro peptidase activity

To evaluate TMPRSS2 inhibitors and provide groundwork for future structure activity relationship (SAR) studies, we established in vitro proteolytic activity and inhibition assays. The generic TTSP

126 fluorogenic peptide substrate Boc-Gln-Ala-Arg-7-aminomethylcoumarine (AMC) was rapidly
127 cleaved by dasTMPRSS2, C-terminal to Arg, thereby releasing AMC product and enabling initial
128 reaction velocities (V_o) measurement within 60 seconds of enzyme addition (Fig. 3a). In Assay
129 Buffer, dasTMPRSS2 had a K_m of (200±80) µM, V_{max} of (0.7±0.2) nmol min^{-1}, k_{cat} of (18±4)s^{-1},
130 k_{cat}/K_m of (5.4±0.2) µM^{-1}min^{-1} and specific activity at (0.22±0.03) µmol min^{-1}mg^{-1} enzyme
131 purified to apparent homogeneity (Fig. 3b). To our knowledge, this level of activity has not been
132 achieved with any previously described recombinant TMPRSS2 enzyme[17–20], and enzyme activity
133 was unaffected by the presence of Ca^{2+}, NaCl concentrations ranging 75-250 mM, EDTA, and
134 tolerant of 2% (v/v) DMSO (Extended Data Fig. 4c) that is encouraging for use in high throughput
135 inhibitor screening campaigns.
136
137 **TMPRSS2 efficiently cleaves the SARS-CoV-2 S protein at the S1/S2 site in vitro**
138 Cells expressing TMPRSS2 have been shown to efficiently cleave the SARS-CoV-1 S protein at
139 S1/S2 (SLLR667↓) and multiple peripheral sites to induce the necessary conformational changes
140 leading to virus-host fusion at the plasma membrane[21,22] (Fig. 1a; Extended Data Fig. 5a). This
141 extensive TMPRSS2 processing has also been linked to periplasmic shedding of the S1 fragment
142 to act as an immune decoy in vivo[22]. For SARS-CoV-2, an acquired multibasic RRAR685↓ S1/S2
143 cleavage sequence was hypothesized to confer preferential cleavage by intracellular furin
144 protease[23], and was corroborated by studies showing that multibasic, peptidomimetic furin
145 inhibitors prevented S1/S2 cleavage and attenuate infection in cellular models[24]. Further studies
146 showed that these inhibitors are promiscuous and disable multiple surface-expressed proteases that
147 process multibasic substrates in addition to furin, and more selective furin inhibitors cannot fully
148 abrogate S activation[25]. Furthermore, furin-deficient cells can still generate S1/S2 cleaved virus,
149 and propagation of SARS-CoV-2 in TMPRSS2-deficient cell lines results in a loss of the
150 multibasic S1/S2 site[26], attenuating viral infectivity towards TMPRSS2+ cells. We sought to
151 characterize TMPRSS2's proteolytic activity towards S1/S2 by incubating recombinant furin
152 and/or dasTMPRSS2 with stabilized SARS-CoV-2 S protein ectodomain with S1/S2 knocked out
153 (RRAR^{685}->GSAS^{685}; HexaPro construct) or with S1/S2 intact (denoted HexaFurin; Extended
154 Data Fig. 5a; Fig. 3c). As expected from previous studies using recombinant, S1/S2 intact S
155 protein, HexaFurin sustained partial S1/S2 cleavage during production in HEK293 cells due to
156 endogenously expressed furin[27] (Fig. 3c). Recombinant furin treatment converted the remaining
157 intact HexaFurin to S1 and S2 band fragments with incubation over 16 hours, but was unable to
158 cleave HexaPro (Fig. 3c; Extended Data Fig. 5b).
159 In contrast, using both the HexaFurin and HexaPro constructs, we observed that dasTMPRSS2
160 could cleave the S protein at 3 distinct sites with variable efficiency (Fig. 3d-e). HexaFurin was
161 cleaved to only the S1 and S2 fragments within 5 minutes of dasTMPRSS2 addition (Fig. 3d),
162 demonstrating the S1/S2 site was best recognized by TMPRSS2 across a minimal incubation.
163 HexaPro, lacking S1/S2, was cleaved across 30 min to generate a larger 150 kDa band, denoted
164 fragment X, and 80 kDa fragment Y when analyzed under non-reducing conditions (Fig. 3e).
165 Reducing conditions revealed an additional cleavage site hidden within fragment X that is spanned
166 by two cysteine residues participating in a disulfide bond, splitting fragment X into 120 kDa
167 fragment X'a and 35 kDa fragment X'b. Exhaustive HexaPro treatment (120 min) completely
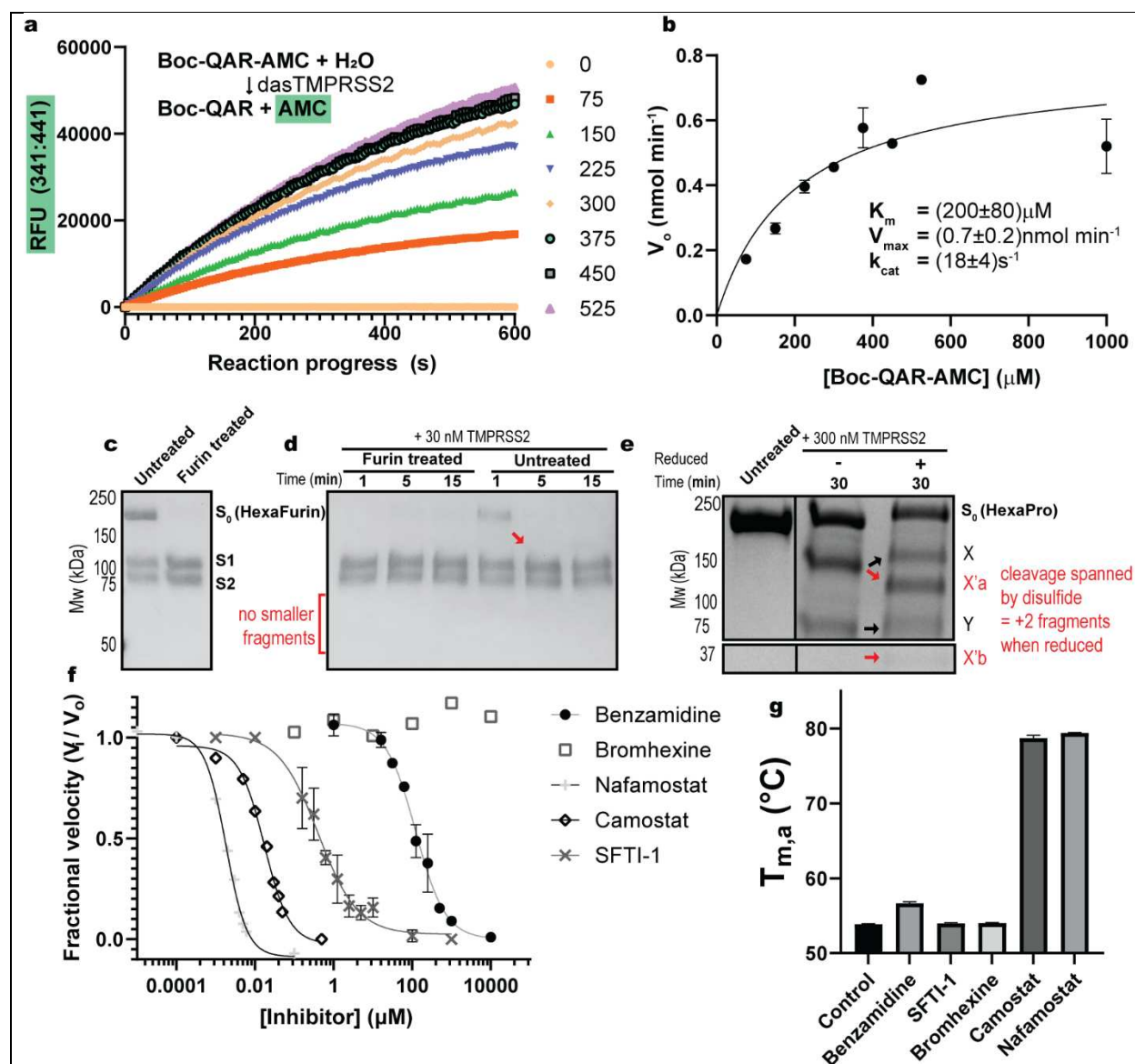168 converted fragment X into X'a and X'b (Extended Data Fig. 6d).
169

Figure 3. dasTMPRSS2 displays robust proteolytic activity towards peptide and SARS-CoV-2 S protein substrates. a The generic Boc-Gln-Ala-Arg-AMC fluorogenic peptide substrate is efficiently cleaved by dasTMPRSS2. Each progress curve was performed in quadruplet. **b** Michaelis-Menten plot of initial reaction velocities for kinetic parameter estimation after curve fitting in GraphPad. **c** S1/S2 intact S protein ectodomain (HexaFurin; S_0) is partially cut at the S1/S2 site to produce S1 and S2 fragments and can be quantitatively converted by recombinant furin treatment over 16 hours. **d** The addition of 30 nM TMPRSS2 to furin treated HexaFurin produces no additional bands, but furin untreated HexaFurin is exhaustively cleaved at S1/S2 within 5 minutes. **e** dasTMPRSS2 cleaves HexaPro at two additional sites peripheral to S1/S2, with the first cleavage producing X and Y band fragments under non-reducing SDS-PAGE conditions. Reducing conditions reveal band fragments X'a and X'b derived from fragment X. **f** dasTMPRSS2 peptidase activity is blocked with varying potencies by clinical protease inhibitors, with no inhibition seen for bromhexine. All data are shown as mean ± s.e.m., $n = 3$ biological replicates **g** Apparent melting temperatures (as determined by differential scanning fluorimetry) are increased for benzamidine, camostat, and nafamostat at 1 µM concentration but are not increased by SFTI-1 or bromhexine. Samples were in triplicate.

170

171   To visualize all of these cleavage sites simultaneously, we treated HexaFurin 30 min with
172   dasTMPRSS2 and compared SDS-PAGE banding to a western blot using an antibody directed
173   towards the S protein receptor binding domain (RBD; Extended Data Fig. 5c). At least 7 bands
174   were observed on reducing SDS-PAGE and the western shows that both the S1 fragment as well
175   as an S1-derived 50 kDa fragment contain the RBD. The banding patterns observed (S1/S2, X/Y,
176   and X'a/X'b cleavages) are consistent with western blot studies monitoring SARS-CoV-1 S
177   protein processing by TMPRSS2 that enables shedding of the S1 fragment[22] to act as an immune
178   decoy.
179
180   **Nafamostat rapidly acylates TMPRSS2 and slowly hydrolyzes**
181   Nafamostat and camostat are serine protease inhibitors under investigation as anti-TMPRSS2
182   COVID-19 therapeutics (Clinical Trial.gov identifiers NCT04583592, NCT04625114). Both are
183   reactive esters that form the same slowly-reversible phenylguanidino covalent complex (evidenced
184   in the enteropeptidase-camostat structure; PDB: 6ZOV) with the catalytic serine residue of trypsin-
185   like serine proteases. Nafamostat and camostat dramatically increased the apparent melting
186   temperature ($T_{M,a}$) of dasTMPRSS2 by (25.5±0.1) and (24.8±0.3) °C, respectively, as measured
187   by Differential Scanning Fluorimetry (DSF)[28] (Fig. 3g) and was a key stabilizing feature to enable
188   protein crystallization (Methods). Nafamostat demonstrated enhanced potency over camostat with
189   IC$_{50}$ values of (1.7±0.2) and (17±4) nM, respectively, with 5 min assay pre-incubation (Fig. 3f).
190   However, IC$_{50}$ values were time-dependent and required further kinetic interrogation to assess
191   their divergent potencies (Extended Data Fig. 6b-c). Nafamostat was 40-fold more potent than
192   camostat with respective k_{inact}/K_i values of (0.024±0.006) and (0.00059±0.00003) s^{-1} nM^{-1}.
193   These results emphasize that single timepoint IC$_{50}$ values are insufficient for evaluating
194   mechanism-based, covalent inhibitors of this highly active protease in SAR studies. As previously
195   identified for matriptase, the nafamostat leaving group, 6-amidino-2-napthol, fluoresces and can
196   be used as a sensitive burst titrant to calculate the concentration of active protease (Extended Data
197   Fig. 4e-f; Methods)[19]. The half-life of the phenylguanidino acyl-enzyme complex was (14.7±0.4)
198   hours as measured by the gradual rescue of dasTMPRSS2 peptidase activity after stoichiometric
199   acylation with nafamostat (Extended Data Fig. 3e-f). Impressively, stoichiometric amounts of
200   nafamostat completely blocked dasTMPRSS2-mediated HexaPro activation over 2 hours
201   (Extended Data Fig. 6d) and are consistent with this drug's ability to potently block SARS-CoV-
202   2 pseudovirus entry to TMPRSS2+ Calu-3[29] and Caco-2[5,20] lung cells.
203
204   Non-covalent trypsin-like serine protease inhibitors benzamidine and sunflower trypsin inhibitor-
205   1 (SFTI-I) were less potent with respective IC$_{50}$ values of (120±20) μM and (0.4±0.2) μM (Fig.
206   3f), and K_i values of (80±10) μM and (0.4±0.2) μM (Extended Data Fig. 7a-b). 6-amidino-2-
207   napthol also disabled dasTMPRSS2 activity with an IC$_{50}$ of (1.6±0.5) μM and K_i of (1.1±0.3) μM
208   (Extended Data Fig. 7a). Bromhexine hydrochloride, another agent under investigation for anti-
209   TMPRSS2 COVID-19 therapy[30,31], showed no inhibition in either the peptidase or HexaPro
210   cleavage assay formats (Extended Data Fig. 7c-d), corroborating reports of its ineffectiveness in
211   blocking SARS-CoV-2 pseudovirus entry[32] and further underscores the need for novel, selective
212   TMPRSS2 inhibitors.
213
214   **Future prospects**
215   We have produced and characterized a source of TMPRSS2 enzyme that will enable rapid inhibitor
216   development as antivirals and thorough molecular interrogation of coronavirus and influenza virus

217 activation. Although nafamostat potently neutralizes TMPRSS2 activity, it is non-selective and
218 disables trypsin-like serine proteases involved in coagulation such as plasmin, FXa, and FXIIa, as
219 well as other TTSPs through its generic arginine-like engagement with the S1 subsite[19,33,34].
220 Furthermore, nafamostat requires continuous intravenous infusion to approach therapeutic
221 concentrations for COVID-19 owing to its short biological half-life of 8 minutes (NCT04418128;
222 NCT04473053). These features, although undesirable as a selective therapeutic, make nafamostat
223 an extremely useful and sensitive reagent for *in vitro* kinetic characterization of trypsin-like
224 proteases, and sufficiently stabilized our protease for crystallization and structural determination.
225 Nevertheless, selective and biologically stable drugs for TMPRSS2 must be explored, and may be
226 achieved through inhibitors engaging the more TMPRSS2-specific S2, S3, and S4 subsites
227 identified in our crystal structure.
228
229 We observed no electron density for the LDLR-A domain of TMPRSS2, despite a similar construct
230 design to that which afforded the TMPRSS13 crystal structure (PDB: 6KD5). The LDLR-A
231 domain of TTSPs is responsible for tethering the protease to the plasma membrane and most
232 TTSPs have a conserved ability to bind calcium. Interestingly, a key Asp residue in TMPRSS13
233 involved in calcium chelation is absent in human and other mammalian TMPRSS2 proteins,
234 substituted instead with His or Gln residues (Extended Data Fig. 8). These data suggest that
235 TMPRSS2 may have lost the ability to bind calcium at this site.
236
237 Our demonstration that TMPRSS2 can cleave the multibasic S1/S2 site of the S protein suggests
238 that instead of conferring furin dependence, the virulent properties of this site may derive from
239 promiscuous recognition and cleavage by airway-expressed TTSPs, which is supported by the
240 demonstrated roles that TMPRSS4[35,36], TMPRSS11d[20,37,38], and TMPRSS13[20,37], which colocalize
241 with ACE2[36], play in enabling SARS-CoV-2 infection across various tissues.
242
243 Our characterization of dasTMPRSS2 did not reveal an obvious mechanism by which the native,
244 membrane-bound enzyme could be autoproteolytically processed peripheral to the activation motif
245 and thereby shed as a soluble enzyme into the extracellular space. However, studies using
246 TMPRSS2-specific antibodies have reported detection of a secreted enzyme product in prostate
247 sera that is expected to play a functional role in pericellular activation[39]. Due to the disulfide-linked
248 nature of activated TMPRSS2, former studies may have mischaracterized the catalytic subunit as
249 a shed SP domain when it would instead resolve to the intact species under non-reducing
250 conditions (Fig. 1b). Thus, a biochemical characterization of these secreted species is required to
251 interpret their activation status and subunit organization, as an active, shed form of TMPRSS2 in
252 the extracellular milieu would have profound pathobiological and therapeutic targeting
253 implications.
254

ACKNOWLEDGEMENTS

271
272 **Author Information**
273 These authors contributed equally: Bryan J. Fraser, Serap Beldar
274
275 **Author Affiliations**
276
277 **Department of Molecular Oncology, British Columbia Cancer Research Institute,**
278 **Vancouver, British Columbia, Canada**
279 Bryan J. Fraser, Daniel Kwon, Ruiyan Tan, Ryan P. Wilson, François Bénard
280
281 **Department of Radiology, University of British Columbia, Vancouver, British Columbia,**
282 **Canada**
283 Bryan J. Fraser, François Bénard
284
285 **Structural Genomics Consortium, University of Toronto, Toronto, Ontario, Canada**
286 Serap Beldar, Almagul Seitova, Ashley Hutchinson, Yanjun Li, Levon Halabelian, Cheryl H.
287 Arrowsmith
288
289 **Department of Biochemistry and Molecular Biology, University of British Columbia,**
290 **Vancouver, British Columbia, Canada**
291 Dhiraj Mannar, Karoline Leopold, Sriram Subramaniam
292
293 **Princess Margaret Cancer Centre, Toronto, Ontario, Canada**
294 Cheryl H. Arrowsmith
295
296 **Department of Medical Biophysics, University of Toronto, Toronto, Ontario, Canada**
297 Cheryl H. Arrowsmith
298
299 **Author Contributions:**
300 F.B., C.H.A., L.H., and S.S. provided project supervision; B.J.F., S.B., A.S., C.H.A., and F.B.
301 conceived the project; B.J.F., S.B., A.S., C.H.A., and L.H. designed the experiments; Y.L. cloned
302 TMPRSS2 protein constructs for expression and Y.L. and D.M cloned SARS-CoV-2 S protein
303 constructs for expression; A.S. and A.H. produced TMPRSS2 protein in insect cells; A.S., A.H.,
304 D.M., K.L. produced SARS-CoV-2 S protein in HEK cells; B.J.F., S.B., A.S., A.H., D.M., and
305 K.L. purified recombinant proteins; B.J.F., S.B., and L.H. crystallized TMPRSS2 and L.H., S.B.,
306 and B.J.F. collected diffraction data; L.H. solved the crystal structure; B.J.F., S.B., and L.H.
307 performed bioinformatic and structural analyses; B.J.F., D.K., R.W., and R.T. performed
308 fluorogenic peptidase activity and inhibitor potency assays and B.J.F. analyzed kinetics; D.K.

309 synthesized, purified, and characterized SFTI-1 peptide; B.J.F., D.K., and S.B. managed inhibitor
310 compound libraries; B.J.F., D.M., and R.T. performed gel-based S protein digestion assays; S.B.
311 and B.J.F. performed DSF assays; B.J.F., S.B., L.H., R.T., and D.M. prepared figures; B.J.F., S.B.,
312 L.H., C.H.A., F.B., A.S., A.H., and Y.L. wrote the manuscript.
313

Competing interests
315 The authors declare no competing interests.
316

Data Availability
318 The coordinates and structure of the phenylguanidino TMPRSS2 acyl-enzyme complex have been
319 deposited in the PDB with accession number 7MEQ on April 7, 2021, and released on April 21,
320 2021. Any other relevant data are available from the corresponding authors upon reasonable
321 request.
322

REFERENCES
324

325 1. Matrosovich, T., Beyerle, M., Klenk, H., Garten, W. & Matrosovich, M. Proteolytic
326 Activation of Influenza Viruses by Serine Proteases TMPRSS2 and HAT from Human
327 Airway Epithelium. **80**, 9896–9898 (2006).
328 2. Böttcher, E. *et al.* Proteolytic Activation of Influenza Viruses by Serine Proteases
329 TMPRSS2 and HAT from Human Airway Epithelium. *J. Virol.* **80**, 9896–9898 (2006).
330 3. Limburg, H. *et al.* TMPRSS2 Is the Major Activating Protease of Influenza A Virus in
331 Primary Human Airway Cells and Influenza B Virus in Human Type II Pneumocytes. *J.*
332 *Virol.* **93**, 1–22 (2019).
333 4. Matsuyama, S. *et al.* Efficient Activation of the Severe Acute Respiratory Syndrome
334 Coronavirus Spike Protein by the Transmembrane Protease TMPRSS2. *J. Virol.* **84**,
335 12658–12664 (2010).
336 5. Hoffmann, M. *et al.* SARS-CoV-2 Cell Entry Depends on ACE2 and TMPRSS2 and Is
337 Blocked by a Clinically Proven Article SARS-CoV-2 Cell Entry Depends on ACE2 and
338 TMPRSS2 and Is Blocked by a Clinically Proven Protease Inhibitor. 271–280 (2020)
339 doi:10.1016/j.cell.2020.02.052.
340 6. Li, J., Zhan, P. & Liu, X. Targeting the entry step of SARS-CoV-2: a promising
341 therapeutic approach. *Signal Transduct. Target. Ther.* **5**, 2019–2020 (2020).
342 7. Paoloni-giacobino, A., Chen, H., Peitsch, M. C., Rossier, C. & Antonarakis, S. E. Cloning
343 of the TMPRSS2 Gene , Which Encodes a Novel Serine Protease with Transmembrane ,
344 LDLRA , and SRCR Domains and Maps to 21q22 . 3. **320**, 309–320 (1997).
345 8. Chen, Y. *et al.* TMPRSS2 , a Serine Protease Expressed in the Prostate on the Apical
346 Surface of Luminal Epithelial Cells and Released into Semen in Prostasomes , Is
347 Misregulated in Prostate Cancer Cells. **176**, 2986–2996 (2010).
348 9. Afar, D. E. H. *et al.* Catalytic Cleavage of the Androgen-regulated TMPRSS2 Protease
349 Results in Its Secretion by Prostate and Prostate Cancer Epithelia. 1686–1692 (2001).
350 10. Yamasaki, Y., Satomi, S., Murai, N., Tsuzuki, S. & Fushiki, T. Inhibition of membrane-
351 type serine protease 1/matriptase by natural and synthetic protease inhibitors. *J. Nutr. Sci.*
352 *Vitaminol. (Tokyo).* **49**, 27–32 (2003).
353 11. Fujii, S. (Received April 21st, 1981). *Biochim. Biophys. Acta* **661**, 342–345 (1981).
354 12. Klezovitch, O. *et al.* Hepsin promotes prostate cancer progression and metastasis. *Cancer*

355   *Cell* **6**, 185–195 (2004).

356   13.   Ohno, A. *et al.* Crystal structure of inhibitor-bound human MSPL that can activate high
357   pathogenic avian in fl uenza. *Life Sci. Alliance* **4**, 1–11 (2021).

358   14.   Perona, J. J. & Craik, C. S. Evolutionary divergence of substrate specificity within the
359   chymotrypsin-like serine protease fold. *J. Biol. Chem.* **272**, 29987–29990 (1997).

360   15.   Boulware, K. T. & Daugherty, P. S. Protease specificity determination by using cellular
361   libraries of peptide substrates (CLiPS). *Proc Natl Acad Sci U S A* . (2006)
362   doi:10.1073/pnas.0511108103.

363   16.   Yap, N. V. L., Whelan, F. J., Bowdish, D. M. E. & Golding, G. B. The evolution of the
364   scavenger receptor cysteine-rich domain of the. **6**, 1–9 (2015).

365   17.   Lucas, J. M. *et al.* The androgen-regulated protease TMPRSS2 activates a proteolytic
366   cascade involving components of the tumor microenvironment and promotes prostate
367   cancer metastasis. *Cancer Discov.* **4**, 1310–1325 (2014).

368   18.   Meyer, D., Sielaff, F., Hammami, M. & Ottcher-friebertsh, E. B. Identification of the first
369   synthetic inhibitors of the type II transmembrane serine protease TMPRSS2 suitable for
370   inhibition of influenza virus activation. **343**, 331–343 (2013).

371   19.   Nimishakavi, S., Raymond, W. W., Gruenert, D. C. & Caughey, G. H. Divergent inhibitor
372   susceptibility among airway lumen-accessible tryptic proteases. *PLoS One* **10**, 1–17
373   (2015).

374   20.   Hoffmann, M. *et al.* Camostat mesylate inhibits SARS-CoV-2 activation by TMPRSS2-
375   related proteases and its metabolite GBPA exerts antiviral activity. *EBioMedicine* **65**,
376   (2021).

377   21.   Reinke, L. M. *et al.* Different residues in the SARS-CoV spike protein determine cleavage
378   and activation by the host cell protease TMPRSS2. *PLoS One* **12**, 1–15 (2017).

379   22.   Glowacka, I. *et al.* Evidence that TMPRSS2 Activates the Severe Acute Respiratory
380   Syndrome Coronavirus Spike Protein for Membrane Fusion and Reduces Viral Control by
381   the Humoral Immune Response. *J. Virol.* **85**, 4122–4134 (2011).

382   23.   Cells, L., Hoffmann, M. & Kleine-weber, H. Short Article A Multibasic Cleavage Site in
383   the Spike Protein of SARS-CoV-2 Is Essential for Infection of Human ll ll Short Article A
384   Multibasic Cleavage Site in the Spike Protein of SARS-CoV-2 Is Essential for Infection of
385   Human Lung Cells. 779–784 (2020) doi:10.1016/j.molcel.2020.04.022.

386   24.   Bestle, D. *et al.* TMPRSS2 and furin are both essential for proteolytic activation of SARS-
387   CoV-2 in human airway cells. **3**, 1–14 (2020).

388   25.   Tang, T. *et al.* Proteolytic Activation of SARS-CoV-2 Spike at the S1/S2 Boundary:
389   Potential Role of Proteases beyond Furin. *ACS Infect. Dis.* **7**, 264–272 (2021).

390   26.   Id, M. S., Uemura, K., Sato, A. & Toba, S. SARS-CoV-2 variants with mutations at the S1
391   / S2 cleavage site are generated in vitro during propagation in TMPRSS2-deficient cells.
392   1–17 (2021) doi:10.1371/journal.ppat.1009233.

393   27.   Gobeil, S. M. *et al.* Article D614G Mutation Alters SARS-CoV-2 Spike Conformation
394   and Enhances Protease Cleavage at the S1 / S2 Junction ll ll D614G Mutation Alters
395   SARS-CoV-2 Spike Conformation and Enhances Protease Cleavage at the S1 / S2
396   Junction. *CellReports* **34**, 108630 (2021).

397   28.   Niesen, F. H., Berglund, H. & Vedadi, M. The use of differential scanning fluorimetry to
398   detect ligand interactions that promote protein stability. *Nat. Protoc.* **2**, 2212–2221 (2007).

399   29.   Hoffmann, M., Schroeder, S., Kleine-weber, H., Müller, M. A. & Drosten, C. Nafamostat
400   Mesylate Blocks Activation of SARS-CoV-2 : New Treatment Option for COVID-19.

401   *Antimicrob Agents Chemother* **64**, 19–21 (2020).

402   30.   Li, T. *et al.* Bromhexine Hydrochloride Tablets for the Treatment of Moderate COVID-
403   19 : An Open-Label Randomized Controlled Pilot Study. *Clin. Transl. Sci.* **13**, 1096–1102
404   (2020).

405   31.   Wang, Y. *et al.* Evaluating the efficacy and safety of bromhexine hydrochloride tablets in
406   treating pediatric COVID-19. *Medicine (Baltimore).* **99**, 0–4 (2020).

407   32.   Shrimp, J. H. *et al.* An Enzymatic TMPRSS2 Assay for Assessment of Clinical
408   Candidates and Discovery of Inhibitors as Potential Treatment of COVID-19. (2020).

409   33.   Hitomi, Y, Ikari, N, Fujii, S. Inhibitory Effect of a New Synthetic Protease Inhibitor
410   (FUT-175) on the Coagulation System. *Haeomstasis* **15**, 164–168 (1985).

411   34.   Muto, S., Imai, M. & Asano, Y. Mechanisms of hyperkalemia caused by nafamostat
412   mesilate. *Gen. Pharmacol.* **26**, 1627–1632 (1995).

413   35.   Zang, R. *et al.* TMPRSS2 and TMPRSS4 mediate SARS-CoV-2 infection of human small
414   intestinal enterocytes. *bioRxiv* **3582**, 1–14 (2020).

415   36.   Wruck, W. & Adjaye, J. SARS-CoV-2 receptor ACE2 is co-expressed with genes related
416   to transmembrane serine proteases, viral entry, immunity and cellular stress. *Sci. Rep.* **10**,
417   1–14 (2020).

418   37.   Kishimoto, M. *et al.* Tmprss11d and tmprss13 activate the sars-cov-2 spike protein.
419   *Viruses* **13**, (2021).

420   38.   Ph, D. Intracellular autoactivation of TMPRSS11A, an airway epithelial transmembrane
421   serine protease. (2020) doi:10.1074/jbc.RA120.014525.

422   39.   Kesic, M. J., Meyer, M., Bauer, R. & Jaspers, I. Exposure to ozone modulates human
423   airway protease/antiprotease balance contributing to increased influenza a infection. *PLoS*
424   *One* **7**, 1–12 (2012).

425
426
427
428
429
430
431
432
433
434
435
436
437
438
439
440
441
442
443
444
445
446

447 **METHODS**
448
449 **Construct design and cloning**
450 A construct encoding residues 109-492 comprising soluble TMPRSS2 ectodomain was amplified
451 by two PCR fragments (Addgene plasmid# 53887) and subcloned into the pFHMSP-LIC C donor
452 plasmid by LIC method. The final construct contained a N-terminal honeybee melittin signal
453 sequence peptide and C-terminal His_8-tag (Fig.1b). Mutations targeting the activation sequence
454 SSQSR255↓IVGGE (arrow indicates the cleavage site) were implemented to replace the
455 SRQSR255 residues with an enteropeptidase-cleavable DDDDK255 graft with two sets of primer
456 pairs (Extended Data Table 1) generating mutations for S251D/R252D/Q253D/S254D/R255K.
457 Plasmid transfer vector containing the TMPRSS2 gene was transformed into *Escherichia coli*
458 DH10Bac cells (Thermo Fisher; Cat# 10361012) to generate recombinant viral bacmid DNA. Sf9
459 cells were transfected with Bacmid DNA using JetPrime transfection reagents (PolyPlus
460 Transfection Inc.; Cat# 114-01) according to the manufacturer's instructions, and recombinant
461 baculovirus particles were obtained and amplified from P1 to P2 viral stocks. Recombinant P2
462 viruses were used to generate suspension culture of baculovirus infected insect cells (SCBIIC) for
463 scaled-up production of TMPRSS2.
464
465 The SARS-CoV-2 Spike ectodomain HexaPro construct was a gift from J. McLellan[1], and the
466 S1/S2 site was restored ($GSAS^{685}$->RRAR) through site-directed mutagenesis with primers in
467 Extended Data Table 1 (HexaFurin construct).
468
469 **Baculovirus mediated dasTMPRSS2 protein production in Sf9 insect cells**
470 Sf9 cells were grown in I-Max Insect Medium (Wisent Biocenter; Cat# 301-045-LL) to a density
471 of $4x10^6$ cells/mL and infected with 20 mL/L of suspension culture of baculovirus infected insect
472 cells prior to incubation on an orbital shaker (145 rpm, 26 ºC).
473
474 **dasTMPRSS2 protein purification**
475 Cell culture medium containing the final secreted protein product AA-[TMPRSS2(109-492)]-
476 EFVEHHHHHHHH was collected by centrifugation (20 min, 10 ºC, 6,000 x g) 4-5 days post-
477 infection when cell viability dropped to 55 - 60%. Media was adjusted to pH 7.4 by addition of
478 concentrated PBS stock, then supplemented with 15 mL/L settled Ni-NTA resin (Qiagen) at a scale
479 of 12 L. Three batch Ni-NTA purifications were used to capture protein, with each round requiring
480 shaking in 2L flasks for 2 hours at 16 ºC (110 rpm), harvesting by centrifugation (5 min 1,000 x
481 g), then transferred to a gravity flow column. Beads were washed with 3 column volumes (CVs)
482 ice-cold PBS prior to elution with PBS supplemented with 500 mM imidazole. Elution samples
483 were concentrated to 4.5 mg/mL using 30 kDa MWCO Amicon filters and overnight zymogen
484 activation was achieved by dialyzing protein 1:1000 against Assay Buffer (25 mM Tris pH 8.0, 75
485 mM NaCl, 2 mM $CaCl_2$) at room temperature in the presence of recombinant enteropeptidase
486 (NEB) at 13 U enzyme per mg TMPRSS2 zymogen. The following day, activated samples were
487 exchanged to SEC buffer (50 mM Tris pH 7.5, 250 mM NaCl), spun down at 17,000 x g, then
488 loaded to a Superdex 75 gel filtration column. Fractions spanning the dominant peak eluting at 80
489 mL (Extended Data Fig. 1) were evaluated for appropriate banding on reducing SDS-PAGE prior
490 to pooling and concentrating. For dasTMPRSS2 enzyme samples, 2 µL aliquots of 10,000x
491 enzyme assay stocks (32 µM) were prepared by concentrating protein to 1.6 mg/mL in Enzyme
492 Buffer (50 mM Tris pH 7.5, 250 mM NaCl, 25% glycerol), then flash-frozen in liquid nitrogen

493 and stored at –80 °C until thawed immediately prior to use for each enzyme assay in order to
494 minimize autoproteolysis and maintain reproducible enzyme concentrations.
495

HexaPro and HexaFurin production and purification
497 Expi293F cells (Life Technologies Cat. # A1435102) were transiently transfected with expression
498 plasmid encoding HexaPro/Furin using FectoPro transfection reagent (Polyplus-transfection® SA,
499 Cat. #116-010) with 5 mM sodium butyrate being added at the time of transfection (Sigma, Cat. #
500 303410). After 4-5 days post-transfection time cells culture was harvested, supernatant cleared by
501 centrifugation, and the pH was adjusted by adding 10x Buffer (50 mM Tris pH 8.0, 150 mM NaCl).
502 Secreted protein was captured by two round of batch absorption (BA) with 4 mL/L of pre-
503 equilibrated Ni Sepharose beads (GE Healthcare, Cat #17-5318-01). The bound beads were
504 transferred to gravity flow column and sequentially washed with 30 CVs Wash Buffer (50 mM
505 HEPES 7.5, 300 mM NaCl, 5% glycerol), followed by Wash Buffer supplemented with 25 mM
506 imidazole. Protein was eluted in Elution Buffer (Wash buffer with 250 mM imidazole) and
507 concentrated using Amicon™ Ultra Centrifugal Filter Units, 15 mL, 100 kDa (Millipore Sigma™
508 Cat# UFC910024) prior to size-exclusion chromatography purification using a Superose 6 Increase
509 10/300 GL (GE Healthcare Cat # 29-0915-96), in a buffer composed of 20 mM HEPES pH 7.5,
510 200 mM NaCl.
511

Protein crystallization and structural determination
513 After size-exclusion purification of activated dasTMPRSS2, samples were pooled and
514 concentrated to 2 mg/mL. Protein was treated with 3:1 nafamostat:dasTMPRSS2 for 10 minutes
515 at room temperature and exchanged into Assay Buffer supplemented with 3:1 nafamostat using 4
516 spin cycles in 30 kDa Amicon MWCO filters (14,000 rpm, 15 min, 4 °C) to remove low Mw
517 autolytic fragments from the 42 kDa enzyme (Extended Data Fig. 1b). Acylated enzyme was then
518 concentrated to 8 mg/mL and centrifuged (14,000 rpm, 10 min, 4 °C) prior to automated screening
519 at 18 °C in 96-well Intelliplates (Art Robin) using the Phoenix protein crystallization dispenser
520 (Art Robbins). Protein was dispensed as 0.3 µL sitting drops and mixed 1:1 with precipitant. The
521 RedWing and SGC precipitant screens were tested and amorphous, non-diffracting crystals were
522 consistently produced when grown over 30% Jeffamine ED-2001 (Hampton Research) with 100
523 mM HEPES pH 7.0. To acquire a diffraction quality crystal, acylated dasTMPRSS2 was treated
524 with 50 U PNGase F (NEB; 37 °C for 45 min) to trim N-glycan branches, then centrifuged (14,000
525 rpm, 4 °C, 10 min) prior to setting 2 µL hanging drops with 1:1 protein: precipitant and grown for
526 10 days. Crystals were then cryo-protected using reservoir solution supplemented with ~5% (v/v)
527 ethylene glycol, and cryo-cooled in liquid nitrogen. X-ray diffraction data were collected on the
528 beamline 24-ID-E at the Advanced Photon Source (APS). Data were processed with XDS[2]. Initial
529 phases were obtained by molecular replacement in Phaser MR[3], using (PDB: 1Z8G) as a starting
530 model. Model building was performed in COOT[4] and refined with Buster[5]. Structure validation
531 was performed in Molprobity[6]. Data collection and refinement statistics are summarized in
532 Extended Data Table 2.
533

Gel electrophoresis and western blotting
535 SDS-PAGE was carried out with 15 µL Mini-Protean (BioRad) or 60 µL Novex Wedgewell
536 (Invitrogen) 4-20% Tris-Glycine gels for 30 min under constant voltage at 200V. Protein samples
537 were mixed with 4x Laemelli buffer (BioRad) and subjected to differential reducing (± 5 mM β-
538 mercaptoethanol; Gibco), then boiling at 95 °C for 5 min in order to probe the covalent nature of

539 protein complexes and subunits. The Precision Plus Protein marker (BioRad) was used as a
540 standard.
541 For SARS-CoV-2 RBD western blotting, SDS-PAGE was carried out as described, followed by
542 wet transfer in Transfer Buffer (25 mM Tris pH 8.3, 192 mM glycine, 20% MeOH (v/v)) to PVDF
543 membrane (80 V, 53 min, 4 °C). Membranes were incubated in Blocking Buffer (5% skim milk
544 in TBST) for 1 hr at room temperature, washed 5x with TBST, then probed overnight with 1/3000
545 mouse anti-RBD primary mAb (Abcam ab277628) solution at 4 °C. Membranes were then washed
546 5x with TBST and probed with 1/5000 FITC-labelled goat anti-mouse IgG secondary pAb (Abcam
547 ab6785) and imaged for fluorescence on the Typhoon FLA7000 biomolecular imager (GE
548 healthcare).
549
550 **Enzyme peptidase and inhibition assays**
551 Peptidase assays with fluorogenic Boc-Gln-Ala-Arg-AMC substrate (Bachem Cat #
552 4017019.0025) were performed in 96-well plates (Greiner Fluotrak) at 200 µL reaction volumes
553 in a FlexStation microplate reader (Molecular Devices) at 24 °C. Fluorescence was monitored with
554 the fastest kinetic read settings across 5 minutes at 341:441 nm excitation:emission and converted
555 to a product AMC concentration using standard curves at each substrate concentration to correct
556 for the inner-filter effect[7] (Extended Data Fig. 4d). All assays contained 2% (v/v) DMSO and
557 initial reaction velocities were tabulated over the linear portion of the first 60 seconds of progress
558 curves.
559 To determine Michaelis Menten kinetic parameters, 50 µL 4x enzyme stock was added through
560 automated addition to microplates containing 150 µL substrate (0.5-1000 µM) in triplicate and
561 initial reaction velocities were plotted against substrate concentration and curve fit using GraphPad
562 Prism.
563 Half-maximal inhibitor (IC$_{50}$) potencies of nafamostat mesylate (MedChemExpress Cat # HY-
564 B0190A), camostat mesylate (MedChemExpress Cat # HY-13512), benzamidine HCl (Sigma Cat
565 # 434760-25G), bromhexine HCl (SelleckChem Cat # S2060), and SFTI-1 were initially
566 determined by pre-incubating dasTMPRSS2 with inhibitor at concentrations ranging from 0.1 nM
567 – 100 µM for 10 min, then enzyme-inhibitor mixes were added to substrate through automated
568 addition. Then, 7 inhibitor concentrations spanning three orders of magnitude across the IC$_{50}$ value
569 were used and inhibitor reaction velocities were normalized to uninhibited enzyme and plotted as
570 one-site dose response curves in GraphPad. The apparent Ki (Ki*) of classical competitive trypsin-
571 like serine protease inhibitors benzamidine and SFTI-1 were determined using Equation 1,

$$K_i^* \approx \frac{IC_{50}}{1 + \dfrac{[S]}{K_M}} \qquad \textbf{(1)}$$

572 Where [S] is the concentration of substrate Boc-QAR-AMC and K_M is the Michaelis constant.
573
574 **Time-dependent IC$_{50}$ measurement and k_{inact}/K_i determination**
575 Camostat IC$_{50}$ curves were generated using 7 concentrations of inhibitor ranging 0.1-1000 nM
576 inhibitor and nafamostat between 0.01-100 nM with a DMSO control as described. The time
577 dependence of inhibitor potencies was measured by using Flexstation Flex kinetic reads that
578 automatically transferred dasTMPRSS2-inhibitor mixes to substrate wells at the indicated pre-
579 incubation timepoints (Extended Data Fig. 6c). For the 10s timepoint, a kinetic read was
580 performed after manual addition of enzyme, followed by substrate, using a multichannel pipette.

581 Kinetic parameters Kiapp and kinact were determined with the simplified Equations 2 and 3,
582 respectively, assuming a one-step kinetic inhibition mechanism, A[8].
583

Mechanism A :	$E + I \xrightarrow{k_1} EI$	
	$$K_i^* \approx \dfrac{t_{50}^{(2)} - t_{50}^{(1)}}{\dfrac{t_{50}^{(2)}}{I_{50}^{(1)}} - \dfrac{t_{50}^{(1)}}{I_{50}^{(2)}}}$$	(2)
	$$k_{inact} \approx \dfrac{1}{t_{50}^{(2)}} \exp\left[\ln\left(\dfrac{K_i^*}{I_{50}^{(2)}} - 1\right) + b\right],$$	(3)

584 where the conversion factor $b = 0.558$ is applied for concentrations in µM and time in s.
585

Active site quantification of dasTMPRSS2
587 The acylation of dasTMPRSS2 by nafamostat and concomitant production of the fluorogenic 6-
588 amidino-2-napthol leaving group was measured by incubating serial log2 enzyme dilutions from
589 6.4-0.8 nM with excess (10 µM) nafamostat, similar to previous efforts with matriptase[9]
590 (Extended Data Fig. 4e-f). Microplate reading at 320: 490 nm excitation:emission were used to
591 calculate the number of dasTMPRSS2 active site residues and calibrate peptidase activity and
592 inhibition assays.
593

Nafamostat inhibition half-life
595 The half-life of the phenylguanidino acyl-enzyme complex after nafamostat treatment was
596 measured for dasTMPRSS2 using methods established for camostat with enteropeptidase[10].
597 Briefly, dasTMPRSS2 (3.2 µM) was mixed with slight excess nafamostat (5 µM or DMSO
598 control) and incubated at room temperature for 20 minutes. After incubation, unbound
599 nafamostat was removed by passage and 3x washes in a 3 kDa MWCO Amicon filter centrifuged
600 at maximum speed. Acylated and untreated dasTMPRSS2 samples were then transferred in
601 quadruplet to a microplate containing either 125 µM or 250 µM substrate (final concentration of
602 3.2 nM enzyme). Fluorescent reads were carried out immediately, analogous to IC_{50} assays, but
603 across a period of 8 hours. The acylated traces were fit to a one-phase association exponential in
604 GraphPad to derive the half-life for activity recovery, normalized to the uninhibited initial
605 reaction velocity.
606

Differential Scanning Fluorimetry
608 Apparent melting temperature ($T_{M,a}$) shifts were measured for various dasTMPRSS2-inhibitor
609 coincubations using SYPRO Orange dye (Life Technologies; cat. S-6650) and monitoring
610 fluorescence at 470:510 nm excitation: emission using the Light Cycler 480 II (Roche Applied
611 Science). Samples were prepared in triplicate in 384 well plates (Axygen; Cat# PCR-384-C; Cat#
612 UC500) at a final volume of 20 µL containing 0.05 mg/mL dasTMPRSS2, 1 µM compound or
613 vehicle control, and 5X SYPRO Orange. Thermal melt curves were generated between 25 °C to
614 95 °C at a gradient of 1 °C /min and plots prepared with the DSFworld application[11] for $T_{M,a}$
615 determination.
616

SARS-CoV-2 S protein activation and inhibition

618 Recombinant SARS-CoV-2 S protein constructs HexaFurin and HexaPro were concentrated to
619 0.5 mg/mL in Assay Buffer and incubated with the indicated concentrations of furin protease
620 (NEB) or dasTMPRSS2. Digestions took place over 16 hours for furin and from 5-120 minutes
621 for dasTMPRSS2. Furin digestions were terminated by the addition of 4 mM EDTA whereas
622 dasTMPRSS2 digestions were terminated with 5 µM nafamostat, then SDS-PAGE samples were
623 immediately prepared with the addition of 4X SDS-PAGE loading buffer and boiled for 5 min at
624 95 °C. 4 µg S protein were loaded per well under each conditions and gels visualized by
625 Coomassie blue staining. For anti-RBD western blotting, 2 µg S protein were loaded per well.
626 For cleavage inhibition assays, dasTMPRSS2 diluted to 320 nM in Assay Buffer was pre-
627 incubated 15 minutes with inhibitor (final 1% DMSO (v/v)) or DMSO control, then assays were
628 started by transfer of enzyme:inhibitor mixes to S protein. S protein:protease mixtures were
629 incubated at room temperature for 2 hours with nafamostat and 30 minutes for bromhexine.
630

Multiple Sequence Alignments
632 Multiple sequence alignments were prepared to compare the human TTSP family members and
633 TMPRSS2 mammalian orthologs. Human TTSP FASTA sequences (isoform 1) were accessed
634 from UniProt and TMPRSS2 orthologs identified with UniProt BLAST. Sequences were aligned
635 with Clustal Omega[12] and annotated with ESPript 3.0[13].
636

Protein Visualization and Property Calculation
638 The structure of dasTMPRSS2 was inspected and compared to other TTSPs using PyMol
639 (Schrodinger) and the Molecular Operating Environment (MOE; Chemical Computing Group)
640 software suite. The exposed hydrophobic patches of TMPRSS2 were calculated using the MOE
641 Protein Patch Analyzer tool[14,15].
642

644 1.   Hsieh, C. *et al.* Structure-based design of prefusion-stabilized SARS-CoV-2 spikes. **1505**,
645   1501–1505 (2020).
646 2.   Kabsch, W. XDS. *Acta Crystallogr.* **D66**, 125–132 (2010).
647 3.   Mccoy, A. J. *et al.* Phaser crystallographic software. *J. Appl. Crystallogr.* **40**, 658–674
648   (2007).
649 4.   Emsley, P. & Lohkamp, B. Features and development of Coot. *Acta Crystallogr.* **D66**,
650   486–501 (2010).
651 5.   Bricogne, G. *et al.* Buster refinement. (2010).
652 6.   Williams, C. J. *et al.* MolProbity : More and better reference data for improved all-atom
653   structure validation. *Protein Sci.* **27**, 293–315 (2017).
654 7.   Liu, Y. *et al.* Use of a fluorescence plate reader for measuring kinetic parameters with
655   inner filter effect correction. *Anal. Biochem.* **267**, 331–335 (1999).
656 8.   Kuzmič, P. A two-point IC 50 method for evaluating the biochemical potency of
657   irreversible enzyme inhibitors. *bioRxiv* (2020)
658   doi:https://doi.org/10.1101/2020.06.25.171207.
659 9.   Nimishakavi, S., Raymond, W. W., Gruenert, D. C. & Caughey, G. H. Divergent inhibitor
660   susceptibility among airway lumen-accessible tryptic proteases. *PLoS One* **10**, 1–17
661   (2015).
662 10. Sun, W. *et al.* Targeting Enteropeptidase with Reversible Covalent Inhibitors To Achieve
663   Metabolic Benefits. 510–521 (2020) doi:10.1124/jpet.120.000219.

664   11.   Wu, T. *et al.* Three Essential Resources to Improve Differential Scanning Fluorimetry (
665   DSF) Experiments. *BioRxiv* (2020).
666   12.   Madeira, F. *et al.* The EMBL-EBI search and sequence analysis tools APIs in 2019.
667   *Nucleic Acids Res.* **47**, W636–W641 (2019).
668   13.   Robert, X. & Gouet, P. Deciphering key features in protein structures with the new
669   ENDscript server. *Nucleic Acids Res.* **42**, W320–W324 (2014).
670   14.   Jetha, A. *et al.* Homology modeling and structure-based design improve hydrophobic
671   interaction chromatography behavior of integrin binding antibodies. *MAbs* **10**, 890–900
672   (2018).
673   15.   Chemical Computing Group. Protein Patch Analyzer and 2D Maps. in *MOE User Guide*
674   (2019).

675
676
677
678
679
680
681
682
683
684
685
686
687
688
689
690
691
692
693
694
695
696
697
698
699
700
701
702
703
704
705
706
707
708
709